Quantum Wave Packet Method for State-to-State Reactive Scattering Calculations on AB + CD → ABC + D Reactions†

Marko T. Cvitaš and Stuart C. Althorpe*

Department of Chemistry, University of Cambridge, Lensfield Road, Cambridge, CB2 1EW, U.K.

Received: December 18, 2008; Revised Manuscript Received: February 10, 2009

We describe a quantum wave packet method for computing the state-to-state quantum dynamics of 4-atom AB + CD → ABC + D reactions. The approach is an extension to 4-atom reactions of a version of the reactant−product decoupling (RPD) approach, applied previously to 3-atom reactions (*J. Chem. Phys.* **2001**, *114*, 1601). The approach partitions the coordinate space of the reaction into separate reagent, strong-interaction, and product regions, using a system of artificial absorbing and reflecting potentials. It employs a partitioned version of the split-operator propagator, which is more efficient than partitioning the (exact) time-dependent Schrödinger equation. The wave packet bounces off a reflecting potential in the entrance channel, which generates a source term; this is transformed efficiently from reagent to product Jacobi coordinates by exploiting some simple angular momentum properties. The efficiency and accuracy of the method is demonstrated by numerical tests on the benchmark OH + H_2 → H_2O + H reaction.

I. Introduction

Accurate quantum reactive scattering calculations give a complete quantum description of the dynamics of a reaction and are thus the ultimate benchmarks against which approximate theories and models of chemical reactivity can be tested. Such calculations have been carried out for a variety of simple gas-phase reactions[1] and have allowed comparisons to be made with experiment[2] at an unprecedented level of detail. This in turn has yielded detailed physical pictures of a variety of fundamental quantum processes, which could not be obtained by any other means. Notable examples of these include the discovery of time delays and quantum bottleneck states in direct reactions,[3,4] and a range of new insights into electronically nonadiabatic processes.[5,6]

Such calculations are computationally very demanding, since they scale exponentially with the number of physical dimensions of the reaction. To date, accurate reactive scattering calculations are restricted to simple reactions involving 3 or 4 atoms. For 3-atom reactions at low collision energies, the most accurate and efficient approach is usually to solve the time-independent version of the nuclear Schrödinger equation, which has the advantage of yielding the complete S-matrix of the reaction (from which all possible scattering observables can be obtained). At higher energies, it is more efficient to solve the time-dependent Schrödinger equation using quantum wave packet propagation, since the latter scales more efficiently with basis size.[1,7] (In particular, it scales linearly with increase in the total angular momentum quantum number *J*.) The wave packet approach also has the advantage of yielding the complete wave function of the reaction immediately. The first reactive scattering calculations on 4-atom systems used time-independent approaches,[8−11] but the superior scaling of the wave packet approach means that the majority of attempts to calculate accurate cross sections and rates have used time-dependent methods.[12−24]

One difficulty that makes reactive scattering calculations particularly demanding is the "coordinate problem".[25] If a coordinate system and basis set are a natural and efficient representation of the dynamics in the reagent arrangement, then they are necessarily an unnatural and inefficient representation in the product arrangement, and vice versa. In a wave packet calculation, there are two ways round this difficulty. One can either halt the calculation when most of the packet is in the strong-interaction region (provided the packet has not spread too much), and then transform the entire wave packet from reagent to product coordinates;[12,13] or one can use the reactant−product decoupling (RPD) approach. The latter was introduced by Peng and Zhang,[26] with further developments made by Kouri, Althorpe, and others.[27,28] The idea behind the RPD approach is to split the time-dependent Schrödinger equation into two or more separate equations, each describing a different region of the reaction. The different regions communicate via artificial absorbing or reflecting potentials, which produce source terms that allow the wave packet from one region to be fed into another region. It must be emphasized that the RPD approach is in principle exact.

In previous work,[28] we developed a version of the RPD approach which decouples the reagent, strong-interaction, and product regions of the calculation. This allows state-to-state scattering properties to be computed very efficiently, including the evolution of the wave packet in the product channel. This last feature allowed us to construct time-dependent wave packets that visualize the scattering into space of competing reaction mechanisms in a number of reactions.[3,29−31] In our previous work,[28] the RPD approach was developed for application to 3-atomic reactions. In the present article, we develop it further for application to 4-atomic reactions of type AB + CD → ABC + D.

Although the overall RPD approach is a general scheme for partitioning the Schrödinger equation of a reaction, its extension from 3- to 4-atomic reactions presents a number of challenges to theory. These include complications arising from the non-unitarity of the basis set-to-grid transformation matrices, and the fact that the reactant-to-product coordinate transformation becomes potentially very time consuming. These theoretical challenges and our solutions to them are discussed in detail in

† Part of the "George C. Schatz Festschrift".

10.1021/jp8111974 CCC: $40.75
Published on Web 03/19/2009

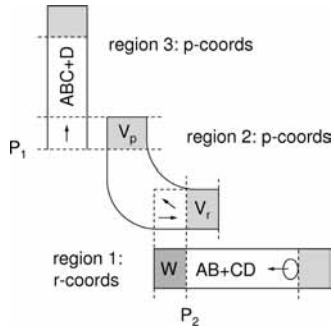

Figure 1. Partitioning of coordinate space for an AB + CD → ABC + D reaction in the reactant−product decoupling (RPD) approach used in this article. The shaded areas correspond to artificial absorbing or reflecting potentials. Note that this diagram is schematic only and that the calculations employ the full 6-dimensional internal coordinate space.

section II. The accuracy and efficiency of the resulting 4-atom RPD propagator are demonstrated by application to the benchmark OH + H_2 reaction in section III. Section IV concludes the paper.

II. Theory

In this section we develop the theory needed to solve the RPD equations for 4-atom reactions in the time domain. We treat all internal degrees of freedom exactly, but limit the total angular momentum of the system to $J = 0$. The extension of the theory to $J > 0$ is straightforward (involving mainly the addition of Coriolis coupling terms), and will be discussed in a later article. We give the general form of RPD equations in section IIA, describe how to solve them using the split-operator propagator in section IIB, discuss the coordinates, basis sets and matrix elements in section IIC, and the extraction of S-matrix elements and state-to-state reaction probabilities in section IID.

A. Further Partitioned Form of the RPD Equations. We use the further partitioned form of the RPD equations given in ref.[28] When applied to an AB + CD → ABC + D reaction, this approach partitions the exact nuclear dynamics Schrödinger equation

$$i\frac{\partial\chi(t)}{\partial t} = H\chi(t) \tag{1}$$

according to

$$\chi(t) = \sum_{\lambda=1}^{3}\chi_\lambda(t) \tag{2}$$

where we have used atomic units such that $\hbar = 1$. The components $\chi_\lambda(t)$ ($\lambda = 1, 2, 3$) describe the reaction dynamics in each of the regions 1−3 shown schematically in Figure 1. They satisfy the RPD equations

$$\begin{aligned} i\frac{\partial\chi_1(t)}{\partial t} &= H\chi_1(t) + W\chi_1(t) \\ i\frac{\partial\chi_2(t)}{\partial t} &= H\chi_2(t) - iV_r\chi_2(t) - iV_p\chi_2(t) - W\chi_1(t) \\ i\frac{\partial\chi_3(t)}{\partial t} &= H\chi_3(t) + iV_p\chi_2(t) \end{aligned} \tag{3}$$

where W is an artificial reflecting potential, placed at the start of the reagent (AB + CD) entrance channel (see Figure 1), and $-iV_r$ and $-iV_p$ are artificial absorbing potentials, placed just outside the "points-of-no-return" P_1 and P_2 (beyond which the scattered wave packet has a negligible probability of re-entering the strong-interaction region). Additional absorbing potentials (not shown in Figure 1 and not included in eq 3) are placed at points-of-no-return at the start of each of the other product channels (corresponding to arrangements AC + BD, AD + BC, ABD + C, ACD + B, BCD + A). Equations 2 and 3 yield the exact $\chi(t)$ in regions 1−3, when the results are converged with respect to P_1 and P_2.

Following ref 28, we employ reagent (AB + CD) Jacobi coordinates in region 1 and product (ABC + D) Jacobi coordinates in regions 2 and 3. The terms $-W\chi_1(t)$ are thus obtained first as a function of reagent coordinates and are then transformed to product coordinates in which form they are used as source terms in the calculation of $\chi_2(t)$. An efficient means of computing the reagent-to-product coordinate transformation is described in section IIE.

B. Solving the RPD Equations in the Time Domain. We solve eqs 2 and 3 by adapting the well-known split-operator propagator of Feit and Fleck.[33] Peng and Zhang[26] have obtained a formal method of solution to the RPD equations in terms of the split-operator propagator. The source terms appear in the propagator as integrals over time, which are solved on an equidistant grid using the trapezium rule. In this work, we use a different approach. Instead of discretizing the formal solution of the RPD equations on a grid in time, we decouple the propagator directly to obtain an exact RPD split-operator propagator.

Let us consider first an implementation of the RPD approach which makes only the partitioning between regions 2 and 3, so that eqs 2 and 3 simplify to

$$\chi(t) = \chi_2(t) + \chi_3(t) \tag{4}$$

and

$$\begin{aligned} i\frac{\partial\chi_2(t)}{\partial t} &= H\chi_2(t) - iV_p\chi_2(t) \\ i\frac{\partial\chi_3(t)}{\partial t} &= H\chi_3(t) + iV_p\chi_2(t) \end{aligned} \tag{5}$$

We can propagate $\chi_2(t)$ using the standard split-operator approach, such that

$$\chi_2(t + \Delta t) = \mathrm{e}^{-V_p\Delta t}\mathrm{e}^{-iH\Delta t}\chi_2(t) \tag{6}$$

We then obtain a propagation formula for $\chi_3(t)$ by subtracting the change that V_p produced in the propagation of $\chi_2(t)$ from $\chi_3(t)$:

$$\chi_3(t + \Delta t) = \mathrm{e}^{-iH\Delta t}\chi_3(t) + (\mathrm{e}^{V_p\Delta t} - 1)\chi_2(t + \Delta t) \tag{7}$$

This ensures that the sum of the propagators on the right-hand sides of eqs 6 and 7 is $\mathrm{e}^{-iH\Delta t}$, and hence that these equations are an exact partitioning of the split-operator propagator, which introduces no additional approximations. As a result, the error in the propagation scales as Δt^3,[33] in contrast to the approach of ref 26 in which the error scales as Δt^2.

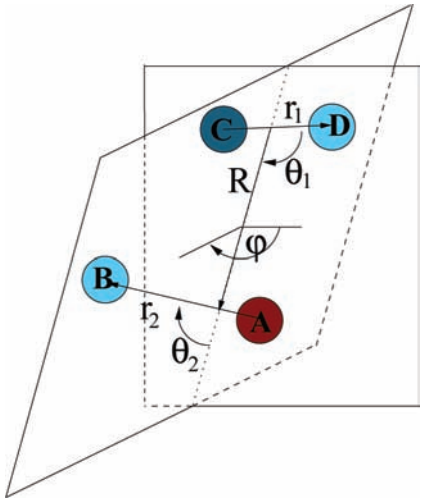

Figure 2. Reagent AB + CD Jacobi coordinate system.

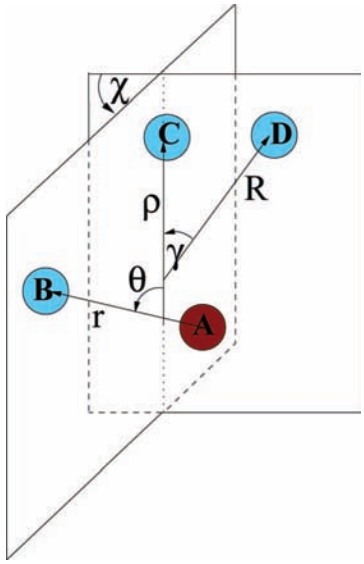

Figure 3. Product ABC + D Jacobi coordinate system.

It is straightforward to generalize the approach of eqs 6 and 7 to treat the full partitioning of eqs 2 and 3, so that analogous expressions are used to implement the partitioning between regions 1 and 2 (with the imaginary absorbing potential $-iV_p$ replaced by the real reflecting potential W). In section III, we compare numerical results obtained using this approach with the approach of ref 26.

C. Reactant and Product Representations. The main advantage of the RPD method is that it allows different coordinate systems and basis sets to be used in the different regions 1−3. We employ diatom−diatom Jacobi coordinates in region 1, which are based on the internal vectors of Figure 2, and atom−triatom Jacobi coordinates in regions 2 and 3, based on the internal vectors of Figure 3. There are a variety of alternative ways of choosing the orthogonal internal vectors of the latter, which lead to a simple kinetic energy operator in the maximally separable form.[37] The vectors shown in Figure 3 were chosen because they represent the nonreacting bond AB using the same vector as in the reactant coordinate system (Figure 2). This has the advantage of reducing the amount of work required to transform the source terms $-W\chi_1(t)$ in eq 3 from reagent to product coordinates. We now describe in detail the different basis sets, Hamiltonian matrix elements and forms of the time-evolution operators used in regions 1−3.

1. Region 1. The time-evolution operator in this region takes the general form of eq 6 and is expressed in terms of the diatom−diatom coordinates of Figure 2. Specifically, the wave packet in this region is propagated according to

$$|\chi(t+\Delta t)\rangle = e^{-iW(R)\Delta t}e^{-iT_R\Delta t/2}e^{-iH_{r1}\Delta t/2} \times e^{-iH_{r2}\Delta t/2}e^{-iT_{ang}\Delta t/2}e^{-iV\Delta t}e^{-iT_{ang}\Delta t/2} \times e^{-iH_{r2}\Delta t/2}e^{-iH_{r1}\Delta t/2}e^{-iT_R\Delta t/2}|\chi(t)\rangle \quad (8)$$

where $W(R)$ is the reflecting potential, $T_R = -1/(2\mu_R R)\cdot(d^2/dR^2)R$ is the radial kinetic energy operator associated with coordinate R, H_{r_i} are the Hamiltonians of the nonrotating diatoms associated with coordinates r_1 and r_2,

$$H_{r_i} = -\frac{1}{2\mu_{r_i} r_i}\frac{d^2}{dr_i^2}r_i + V(r_i) \quad (9)$$

V is the interaction potential [i.e., the total potential energy minus the diatom potentials $V(r_1)$ and $V(r_2)$], and T_{ang} is the kinetic operator associated with the angles θ_1, θ_2, and φ defined in Figure 2.

The primary representation[50] of the wave packet in region 1 is

$$|\chi(t) = \sum_{l,v_1,v_2,j_1,j_2,k} \chi(n, v_1, v_2, j_1, j_2, k, \epsilon|t)|R_n\rangle|v_1\rangle|v_2\rangle|j_1, j_2, k, \epsilon\rangle \quad (10)$$

where $\chi(...|t)$ are time-dependent expansion coefficients and $|R_n\rangle$, $|v_i\rangle$, $|j_1, j_2, k, \epsilon\rangle$ are basis functions associated with coordinates R, r_i and $(\theta_1, \theta_2, \varphi)$, respectively. We now define each of these sets of basis functions in turn.

The basis functions $|R_n\rangle$ are given by

$$\langle R|R_n\rangle = \delta(R - R_n)\sqrt{\Delta R}/R \quad (11)$$

where $\delta(R)$ is a distributed approximating functional (DAF) evaluated over an equidistant mesh of R_n grid points, with spacing ΔR. [A DAF is a localized (analytic) functional approximation to the Dirac- δ function.][54] The radial kinetic energy term in eq 8 is a banded matrix in the DAF basis and its elements are known analytically. The action of the radial kinetic term on a vector in a DAF basis is a convolution, discretized on the grid R_n,

$$e^{-iT_R\Delta t}\chi(n) = \sum_{n'}\Delta R[e^{-iT_R\Delta t}\delta(R_n - R_{n'})]\chi(n') \quad (12)$$

which can be evaluated efficiently using fast Fourier transforms (FFT).[46] All other terms in eq 8 are diagonal in the DAF basis.

The basis functions $|v_i\rangle$ are the eigenstates of the rotationless diatom Hamiltonians, H_{r_i}, with eigenvalues ϵ_{v_i}. This basis is limited by the truncation parameter $v_{max,i}$, determined through numerical convergence. To evaluate the terms involving T_{ang} and V in eq 8, the basis $|v_i\rangle$ is transformed to the discrete variable representation (DVR) obtained by diagonalizing the coordinate matrix.[51]

As in other recent work on 4-atom systems,[14,21] our treatment of the angular problem follows that of Gatti et al.[52,53] and

Mladenović.[37] The basis functions $|j_1, j_2, k, \epsilon\rangle$ are defined with respect to the angular momentum operators which appear in the angular kinetic energy operator

$$\hat{T}_{\text{ang}} = \frac{\hat{\mathbf{l}}^2}{2\mu_R R^2} + \frac{\hat{\mathbf{j}}_1^2}{2\mu_{r_1} r_1^2} + \frac{\hat{\mathbf{j}}_2^2}{2\mu_{r_2} r_2^2} \tag{13}$$

where the μ-terms are the reduced masses associated with the radial coordinates, $\hat{\mathbf{l}}$ is the diatom−diatom orbital angular momentum, and $\hat{\mathbf{j}}_i$ is the rotational angular momentum of diatom i. Let us first construct angular momentum basis functions which are eigenfunctions of the coupled angular momentum operator $\hat{\mathbf{j}}_{12} = \hat{\mathbf{j}}_1 + \hat{\mathbf{j}}_2$ and the total angular momentum $\hat{\mathbf{J}} = \hat{\mathbf{l}} + \hat{\mathbf{j}}_{12}$. These functions can be constructed in either the space-fixed or in a body-fixed frame, where the latter is oriented such that the z axis points along the $\mathbf{R}$ vector and $\mathbf{r}_1$ lies in the positive-x half of the xz plane. For $J = 0$, the space-fixed and body-fixed functions are identical to within a phase factor, and can be written[56]

$$|J, M; l, j_1, j_2, j_{12}\rangle = (-1)^{j_{12}} |J, M; \Omega, j_1, j_2, j_{12}\rangle \tag{14}$$

where M is the projection of J on the space-fixed z axis, and Ω is the projection of J and $l = j_{12}$ on the body-fixed z axis (and $J = M = \Omega = 0$). The angular basis functions $|J, M; \Omega, j_1, j_2, j_{12}\rangle \equiv |j_1, j_2, j_{12}\rangle$ are thus eigenstates of $\hat{\mathbf{j}}_1^2$, $\hat{\mathbf{j}}_2^2$, and $\hat{\mathbf{j}}_{12}^2$, and of the parity operator, with parity eigenvalue

$$\epsilon = (-1)^{j_1 + j_2 + j_{12}} \tag{15}$$

We will refer to these functions as the "coupled" basis functions.

The primary basis functions $|j_1, j_2, k, \epsilon\rangle$ of eq 10 are linear combinations of the coupled basis functions, to which they are related by the orthogonal transformation

$$|j_1, j_2, j_{12}\rangle = \sum_k \langle j_1 - k, j_2 k | j_{12} 0\rangle (-1)^k |j_1, j_2, k, \epsilon\rangle \tag{16}$$

where $\langle ..., ... | ... \rangle$ are Clebsch−Gordan coefficients.[47] The index k is positive only and is equal to the absolute value of the projection of the diatomic angular momenta onto the diatom−diatom axis $\mathbf{R}$. The explicit functional form of $|j_1, j_2, k, \epsilon\rangle$ is

$$\langle \theta_1, \theta_2, \phi | j_1, j_2, k, \epsilon\rangle = \Theta_{j_1 k}(\theta_1)\Theta_{j_2 k}(\theta_2) \frac{1}{\sqrt{2\pi(1 + \delta_{k0})}} [e^{ik\varphi} + \epsilon e^{-ik\varphi}] \tag{17}$$

where Θ_{jk} are associated Legendre functions.[47] In numerical calculations, we limit the size of the basis to $j_1 \le j_{1,\max}$ and $j_2 \le j_{2,\max}$, where the truncation parameters $j_{1,\max}$ and $j_{2,\max}$ are determined by numerical convergence.

To evaluate the action of $e^{-iT_{\text{ang}}\Delta t/2}$ in eq 8, we transform the wave packet from the primary to the coupled representation (using eq 16) in which this operator is diagonal.

To evaluate the action of $e^{-iV\Delta t}$, we transform from the primary to a direct-product generalized DVR (GDVR) basis, $|\theta_{1,\alpha}\rangle |\theta_{2,\beta}\rangle |\varphi_\gamma\rangle$,[44,45] in which $e^{-iV\Delta t}$ is taken to be diagonal. This last assumption is equivalent to remaining in the primitive basis and evaluating the matrix elements over $e^{-iV\Delta t}$ by numerical quadrature. The points $\theta_{1,\alpha}$, $\theta_{2,\beta}$ are Gauss−Legendre quadrature points with associated weights w_α, w_β, and the points φ_γ are equally spaced.

The transformation from the primary basis to the GDVR is performed in three steps, which transform each of the angular degrees of freedom in turn. The first step is the transformation of j_1 to $\theta_{1,\alpha}$. For each j_2 and k, the angular basis is transformed according to

$$|\theta_{1,\alpha}\rangle |j_2, k\rangle = \sum_{j_1} T^{(k)}_{j_1\alpha} |j_1, j_2, k, \epsilon\rangle \tag{18}$$

where a different transformation matrix is used for each k, given by

$$T^{(k)}_{j_1\alpha} = \sqrt{w_\alpha}\Theta_{j_1 k}(\theta_{1,\alpha}) \tag{19}$$

The second step is the analogous transformation of j_2 to $\theta_{2,\beta}$, for which the transformation matrix is given by eq 19 with the labels 1 and 2 exchanged.

The third step is the transformation of k to φ_γ. The latter are distributed over an equally spaced grid, defined by

$$\varphi_\gamma = \gamma \frac{2\pi}{2N_\varphi + 1}, \qquad \gamma = \begin{cases} 0, ..., N_\varphi & \text{if } \epsilon = +1 \\ 1, ..., N_\varphi & \text{if } \epsilon = -1 \end{cases} \tag{20}$$

where

$$N_\varphi \ge \min(j_{1,\max}, j_{2,\max}) \tag{21}$$

The associated weights are

$$\sqrt{w_\gamma} = T^{(\pm)}_{k,\gamma} / \langle \varphi_\gamma | k, \epsilon\rangle = \frac{1}{\sqrt{1 + \delta_{\gamma 0}}} \sqrt{\frac{2\pi}{2N_\varphi + 1}} \tag{22}$$

and the transformation matrices are

$$T^{(+)}_{k\gamma} = \frac{2}{\sqrt{2N_\varphi + 1}} \frac{\cos k\varphi_\gamma}{\sqrt{(1 + \delta_{k0})(1 + \delta_{\gamma 0})}} \tag{23}$$

$$T^{(-)}_{k\gamma} = \frac{2}{\sqrt{2N_\varphi + 1}} \sin k\varphi_\gamma \tag{24}$$

for positive and negative parity eigenvalues, respectively.

The sequence of transformations from the primary basis to the GDVR can thus be summarized as

$$|j_1, j_2, k\rangle \leftarrow T^{(k)}_{j_1\alpha} \rightarrow |\theta_{1,\alpha}\rangle |j_2, k\rangle \leftarrow T^{(k)}_{j_2\beta} \rightarrow |\theta_{1,\alpha}\rangle |\theta_{2,\beta}\rangle |k\rangle \ ... \leftarrow T^{(\epsilon)}_{k\gamma} \rightarrow |\theta_{1,\alpha}\rangle |\theta_{2,\beta}\rangle |\varphi_\gamma\rangle \tag{25}$$

The primary basis is a nondirect product representation, as the range of k is limited by $\min(j_1, j_2)$, and the GDVR is a direct product, and therefore larger in size. The overall transformation between the representations is thus nonunitary. This is not a drawback when the basis is sufficiently large to yield numerically converged results, since then $e^{-iV\Delta t}$ is evaluated sufficiently

accurately to preserve the norm of the wave packet. When the basis set is not sufficiently large (i.e., in a numerically unconverged calculation), then the inaccuracy in the norm of the wave packet can be removed by renormalizing the wave packet as described in ref 15.

2. Region 2. The time-evolution operator in region 2 is expressed in terms of atom−triatom coordinates and takes the form,

$$|\chi(t+\Delta t)\rangle = e^{-V_p(R)\Delta t} e^{-iT_R\Delta t/2} e^{-iT_\rho\Delta t/2} \times e^{-iH_r\Delta t/2} e^{-iT_{ang}\Delta t/2} e^{-iV\Delta t} e^{-iT_{ang}\Delta t/2} e^{-iH_r\Delta t/2} \times e^{-iT_\rho\Delta t/2} e^{-iT_R\Delta t/2} |\chi(t)\rangle + |s(t+\Delta t)\rangle \quad (26)$$

where T_R and T_ρ are the radial kinetic energy operators of the same form as in region 1, associated with the bond-breaking and bond-forming radial coordinates R and ρ; H_r is the Hamiltonian of the nonrotating diatom associated with the coordinate r; V is the interaction potential [i.e., the total potential energy minus the diatom potential $V(r)$], and T_{ang} is the kinetic operator associated with the angles (γ,θ,χ). Note that the absorbing potential V_p is treated separately from the other absorbing potentials (which are included in V), since V_p is used to generate the source terms for region 3. The function $|s(t+\Delta t)\rangle$ is the source term $-W\chi_1(t)$ of eq 3, which is interpolated onto the atom−triatom coordinates of region 2 from the diatom−diatom coordinates of region 1. Details of the interpolation procedure are given in section 2E.

The primary representation of the wave packet in region 2 is

$$|\chi(t)\rangle = \sum_{n,m,v,L,j,\kappa} \chi(n,m,v,L,j,\kappa|t)|R_n|\rho_m\rangle|v\rangle|L,j,\kappa,\epsilon\rangle \quad (27)$$

where $\chi(...|t)$ are time-dependent expansion coefficients, and $|R_n\rangle$, $|\rho_m\rangle$, $|v\rangle$, and $|L, j, \kappa, \epsilon\rangle$ are the basis functions associated with coordinates R, ρ, r and (γ, θ, χ), respectively.

The basis sets $|R_n\rangle$, $|\rho_m\rangle$ consist of equally spaced DAFs, as used for the radial degrees of freedom in region 1 (see above). The action of the kinetic energy operators $e^{-iT_R\Delta t/2}$ and $e^{-iT_\rho\Delta t/2}$ is evaluated efficiently using fast Fourier transforms, as described in eq 12.

The basis functions $|v\rangle$ are the same vibrational basis functions as the functions $|v_2\rangle$ used in region 1 and are thus the vibrational eigenstates of an isolated AB bond. However, the truncation parameter v_{max} is in general different from the parameter $v_{max,2}$ of region 1. As in region 1, the basis $|v\rangle$ is transformed to the DVR when evaluating the action of $e^{-iH_r\Delta t/2}$.

The basis functions $|L, j, \kappa, \epsilon\rangle$ are defined with respect to the angular momentum operators which appear in the angular kinetic energy operator,

$$T_{ang} = \frac{\hat{\mathbf{N}}^2}{2\mu_R R^2} + \frac{\hat{\boldsymbol{\lambda}}^2}{2\mu_\rho \rho^2} + \frac{\hat{\mathbf{j}}^2}{2\mu_r r^2} \quad (28)$$

where the μ-terms are the reduced masses associated with the radial coordinates, and $\hat{\mathbf{N}}$, $\hat{\boldsymbol{\lambda}}$ and $\hat{\mathbf{j}}$ are the angular momentum operators associated with the vectors $\mathbf{R}$, $\boldsymbol{\rho}$, and $\mathbf{r}$. As in region 1, we define first a coupled basis. The coupled angular momentum operator is denoted $\hat{\mathbf{L}} = \hat{\boldsymbol{\lambda}} + \hat{\mathbf{j}}$, and the total angular momentum operator $\hat{\mathbf{J}} = \hat{\mathbf{N}} + \hat{\mathbf{L}}$. We define a body-fixed frame such that the z axis points along the $\mathbf{R}$ vector, and $\boldsymbol{\rho}$ is in the positive x half of the xz plane. For $J = 0$, the basis functions in the space-fixed and body-fixed frame differ only by a phase factor $(-1)^L$. We then define the body-fixed coupled angular basis functions, $|J, M; \Omega, L, \lambda, j\rangle \equiv |L, \lambda, j\rangle$, to be eigenstates of $\hat{\mathbf{L}}^2$, $\hat{\boldsymbol{\lambda}}^2$, and $\hat{\mathbf{j}}^2$, and of the parity operator, with parity eigenvalue

$$\epsilon = (-1)^{L+\lambda+j} \quad (29)$$

As our primary basis, we use the parity-adapted primitive functions $|L, j, \kappa, \epsilon\rangle$, which are related to the coupled basis functions by

$$|L,\lambda,j\rangle = \sum_\kappa \sqrt{2-\delta_{\kappa 0}}\sqrt{\frac{2\lambda+1}{2L+1}}(-1)^{L+\lambda+j}\langle\lambda 0, j\kappa|L\kappa\rangle|L,j,\kappa,\epsilon\rangle \quad (30)$$

where κ is the quantum number associated with the projection of angular momenta L and j onto the ρ axis. The functional form of the $|L, j, \kappa, \epsilon\rangle$ is[57]

$$\langle\gamma,\theta,\chi|L,j,\kappa,\epsilon\rangle = \epsilon\Theta_{L-\kappa}(\gamma)\Theta_{j\kappa}(\theta)\frac{1}{\sqrt{2\pi(1+\delta_{\kappa 0})}}[e^{i\kappa\chi} + \epsilon e^{-i\kappa\chi}] \quad (31)$$

The action of $e^{-iT_{ang}\Delta t/2}$ on the wave packet is evaluated by transforming the wave packet from the primary to the coupled-basis representation, in which this operator is diagonal. The action of $e^{-iV\Delta t}$ is evaluated by transforming to a GDVR, using a 3-step transformation analogous to eq 25 of region 1.

3. Region 3. The wave packet in region 3 is represented in the same atom−triatom coordinate system as that used in region 2. The basis set is also the same as in region 2, except for the basis associated with the ρ coordinate. For the latter, the DAF basis of region 2 is replaced by a basis which consists of the eigenstates of a rotationless diatom, whose potential energy curve is taken to be the ρ-dependence of the asymptotic ABC triatomic potential energy surface, minimized with respect to r and θ. The corresponding DVR is used to evaluate the functions of ρ that occur in $e^{-iT_{ang}\Delta t/2}$ and $e^{-iV\Delta t}$.

4. Remarks on Computational Efficiency. The propagation scheme just described requires storage of two large arrays: the wave packet in the primary representation, and the potential energy surface on the GDVR grid. Unlike the primary basis set, the GDVR grid is a direct product representation. Hence the GDVR grid is much larger than the primary basis, and the transformation of the wave packet to the direct-product grid is the main bottleneck in the propagation. For this reason the potential energy term $e^{-iV\Delta t}$ is placed in the middle of the split-operator formulas of eqs 8 and 26, so that it only has to be evaluated once per time step.

The GDVR representation of the (6-dimensional) potential surface would occupy a large volume of computer memory, were it necessary to store the entire surface. Fortunately, one can evaluate the action of $e^{-iV\Delta t}$ efficiently with most of the potential surface stored on disk. The trick is to read in the potential as a function of the angular degrees of freedom at just one point $(R_\alpha, \rho_\beta, r_\gamma)$ on the three-dimensional radial grid. One can then evaluate the action of $e^{-iV\Delta t}$ via the primary basis-to-GDVR transform, before moving on to the next point on the radial grid.

As mentioned in the Introduction, the RPD approach of this paper was applied previously to triatomic reactions.[28] These earlier calculations used the Chebyshev propagator of Tal-Ezer and Kosloff,[32] which is probably the most accurate propagator available.[55] However, the Chebyshev propagator has the disadvantage of requiring additional applications of the artificial absorbing potentials,[27] which would require two additional primary basis-GDVR transformations per time step. Another disadvantage of the Chebyshev propagator is that it requires the storage of two wave packets rather than one. The split-operator approach described above is thus about three times faster and requires half the memory of the Chebyshev approach.[58]

The reader may ask why we have used the primitive basis sets $|j_1, j_2, k, \epsilon\rangle$ and $|L, j, \kappa, \epsilon\rangle$ as the primary representations of the wave packet, instead of the coupled basis sets $|j_1, j_2, j_{12}\rangle$ and $|L, \lambda, j\rangle$. Use of the latter would make $e^{-iT_{ang}\Delta t/2}$ diagonal, which would reduce the number of transformations between the coupled and primitive basis sets from four to two per time step (where the latter two transformations would be required to transform to and from the GDVR representation when evaluating $e^{-iV\Delta t}$). However, it is possible to implement the primitive basis in such a way that it is never necessary to evaluate the transformation to the coupled basis directly. One replaces the exponential operator $e^{-iT_{ang}\Delta t/2}$ by its Crank−Nicholson approximation $(1 - iT_{ang}\Delta t/4)/(1 + iT_{ang}\Delta t/4)$. The matrix T_{ang} is tridiagonal in the primitive bases. For example, in region 1, it takes the form

$$\mathbf{l}^2|j_1,j_2,k\rangle = [j_1(j_1+1) + j_2(j_2+1) - 2k^2]|j_1,j_2,k\rangle - \sqrt{1+\delta_{k,0}}c_+(j_1,k)c_+(j_2,k)|j_1,j_2,k+1\rangle - \sqrt{1+\delta_{k,1}}c_-(j_1,k)c_-(j_2,k)|j_1,j_2,k-1\rangle \quad (32)$$

where

$$c_\pm(j,k) = \sqrt{j(j+1) - k(k\mp 1)} \quad (33)$$

As a result, one can compute the action of $e^{-iT_{ang}\Delta t/2}$ on the wave packet by solving a set of sparse linear equations, which scales as n_{cp}, rather than n_{cp}^2 (where n_{cp} is the dimension of the transformation matrix between the coupled and primitive representations). It was shown in ref 48 that this combination of Crank−Nicholson and split-operator approaches is stable and accurate and has the same scaling with time step (Δt^3) as the standard split-operator approach.

D. Partitioning Potentials. Here we give details of the (artificial) partitioning potentials W, $-iV_p$, and $-iV_r$ used in eq 3. The reflecting potential W is designed to prevent the wave packet from entering the strong-interaction region, and to provide the source terms $-W\chi_1(t)$ of eq 3, which are used to initiate the wave packet propagation in region 2. It is important to make W as narrow as possible to reduce the effort needed to interpolate the source terms from the diatom−diatom coordinates of region 1 to the atom−triatom coordinates of region 2. There is no need to include any angular or vibrational dependence in W, which is taken to be independent of all coordinates except the diatom−diatom radial coordinate R. The term $e^{-iW(R)\Delta t}$ of eq 8 is thus diagonal in the primary basis set of DAF functions $|R_n\rangle$, and is easy to evaluate.

The explicit functional form of $W(R)$ is

$$W(R) = \frac{W_{ramp}}{2}[\tanh s_w(R_w - R) + 1] \quad (34)$$

where W_{ramp}, R_w and s_w are numerical parameters, determined as follows. The height parameter W_{ramp} must be sufficiently large, and the position parameter R_{wall} sufficiently far from the grid boundary, that $W(R)$ reflects the whole of the incoming wave packet with zero transmission. Within these constraints, R_w should be made as small as possible, as this reduces the distance that the region 2 grid extends along the reagent channel, which in turn reduces the size of the region 2 basis set.[61] The parameter s_w controls the steepness of W on the reactant side; W should be as steep as possible (to keep the source terms as narrow as possible), without being so steep as to induce oscillations in the reflected packet that have too high a frequency to be captured adequately by the reagent-to-product interpolation of the source terms. We discuss the interpolation in section IIE.

The partitioning potential $-iV_p$ is taken to be a transmission-free absorbing potential, of the form[38,39]

$$-iV_p(R) = -i\frac{1}{2\mu_R}\left(\frac{2\pi}{\Delta r_{abs}}\right)^2 y(x) \quad (35)$$

where R is the ABC−D radial separation (Figure 3), and

$$y(x) = \frac{4}{(c-x)^2} + \frac{4}{(c+x)^2} - \frac{8}{c^2}$$
$$x = c(r - r_{abs})/\Delta r_{abs} \quad (36)$$

with $c \approx 2.62$. The advantage of this form of $-iV_p$ is that it has only one numerical parameter, the width Δr_{abs}, that needs to be determined by numerical convergence tests. It is also necessary to converge the calculation with respect to the plane-of-no-return (illustrated schematically in Figure 1), which is done by moving r_{abs} in the direction of increasing ABC−D separation until the results have converged. As with the reflecting potential $W(R)$, $-iV_p(R)$ depends only on the radial coordinate R, so that $e^{-V_p(R)\Delta t}$ of eq 26 is diagonal in the DAF basis.

The same form as eq 35 is used for the partitioning potential $-iV_r$, except that R is now the diatom−diatom radial distance (Figure 2), and is therefore a function of all the atom−triatom radial coordinates except r. This does not require extra work, since we do not need to generate source terms from this partitioning potential, and hence do not need to include it in the form of eq 6. The potential $-iV_r$ is therefore included in the interaction potential V. The other absorbing potentials, used to absorb the packet at the start of the other product channels, and to prevent it from hitting the region 1 and region 3 grid boundaries, are treated in the same way as $-iV_r$.

E. Reagent-to-Product Coordinate Transformation. At every iteration that the wave packet in region 1 overlaps the reflecting potential, eq 34, we need to transform the source term $|s(t)\rangle$ in eq 26 from the region 1 (diatom−diatom) coordinates to region 2 (atom−triatom) coordinates. Using eq 7, the source term expansion coefficients in the basis set of region 1 are

$$s(n_{reg1}, v_1, v_2, j_1, j_2, k) = (e^{iW(R_{n_{reg1}})\Delta t} - 1)\chi(n_{reg1}, v_1, v_2, j_1, j_2, k) \quad (37)$$

We denote the transformed source term expansion coefficients in region 2 by $s(n_{reg2}, m, v, L, j, \kappa)$, where the index n on the

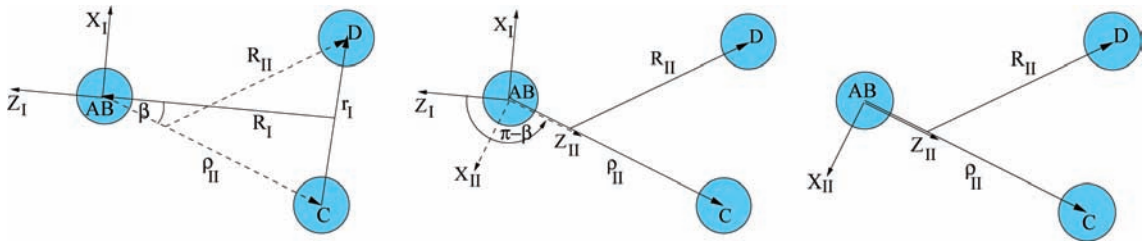

Figure 4. Diagram showing the reagent-to-product coordinate transformation applied to the source terms $-W\chi_1(t)$. All variables are defined in the text. Step 1 in the transformation procedure is described by the leftmost and central figures. Step 2 is decribed by the central and rightmost figures.

region 2 grid is distinguished from the n index on region 1 grid in eq 37 by the subscript. The transformation is accomplished in four steps as follows.

We first note in Figures 2 and 3 that atoms C and D and the center of mass of the AB molecule lie on a plane which contains the vectors ($\mathbf{R}_{reg2}$, $\boldsymbol{\rho}$) and ($\mathbf{R}_{reg1}$, $\mathbf{r}_1$). The two pairs of internal vectors are related through the usual atom−diatom kinematic rotations. So transformation between them is independent of the orientation and bond length of AB. Next, we determine all the region 2 triplets ($R_{n,reg2}$, ρ_m, γ_α) that map onto ($R_{reg1}(i)$, $r_1(i)$, $\theta_1(i)$) on the area covered by the reflecting potential in region 1; we label the triplets collectively by $i = (n, m, \alpha)$.

In the first step of the transformation procedure, shown in Figure 4, we evaluate the source term in the intermediate representation spanned by the basis functions $|(R_{reg2}, \rho, \gamma)_i\rangle|v_2\rangle|j_2, k\rangle$, where $|(R_{reg2}, \rho, \gamma)i\rangle$ is the grid basis (DAF/DAF/DVR) of region 2 and the remaining part describes the AB molecule in the finite basis representation (FBR) of region 1. For each (v_2, j_2, k) of region 1 basis, the source coefficients in the intermediate basis are obtained using

$$s(i, v_2, j_2, k) = \sum_{n_{reg1}, v_1, j_1} U(i, n_{reg1})U(i, v_1)U(i, j_1)s(n_{reg1}, v_1, v_2, j_1, j_2, k) \quad (38)$$

where the overlap matrices are

$$U(i, n_{reg1}) = \delta(R_{reg1}(i) - R_{n_{reg1}})\sqrt{\Delta R_{reg1}\Delta R_{reg2}}\frac{R_{reg2}(i)}{R_{reg1}(i)} \quad (39)$$

$$U(i, v_1) = \psi_{v_1}(r_1(i))\sqrt{\Delta\rho}\frac{\rho(i)}{r_1(i)} \quad (40)$$

$$U(i, j_1) = \sqrt{w_{\alpha(i)}}\Theta_{j_1 k}(\theta_1(i)) \quad (41)$$

In the above formulas, $\delta(R)$ is a DAF, grid spacings and weights are appropriate for the region 2 basis, and $\psi_{v_1}(r_1)/r_1$ are the CD (vibrational) basis functions in region 1.

The rotational basis functions of the AB molecule in the intermediate representation, $|j_2, k\rangle$, are still defined with respect to the diatom−diatom BF frame. We need to re-express them in terms of the rotational basis $|j, \kappa\rangle$ in region 2, which is defined with respect to the molecular frame of ABC molecule, with z axis along ρ, and R_{reg2} in the negative x half of the xz plane. This is accomplished by a rotation about the common y axis by $\pi - \beta$, where

$$\beta = \cos^{-1}\left(\frac{R_{reg1}^2 + \rho^2 - \left(\frac{m_D}{m_{CD}}r_1\right)^2}{2R_{reg1}\rho}\right) \quad (42)$$

The parity-adapted transformation rule for the source coefficients is explicitly orthogonal and reads

$$s(i, v_2, j, \kappa) = \sum_k \frac{1}{\sqrt{1+\delta_{\kappa 0}}}\frac{1}{\sqrt{1+\delta_{k0}}}[d^{j_2}_{\kappa k}(\pi - \beta(i)) + \epsilon(-1)^\kappa d^{j_2}_{\kappa -k}(\pi - \beta(i))]s(i, v_2, j_2, k) \quad (43)$$

where $d^{j_2}_{\kappa k}(\beta)$ are the reduced Wigner rotation matrices and the rotation angles $\beta(i)$ are determined for each triplet ($R_{reg2}(i)$, $\rho(i)$, $\gamma(i)$) using eq 42. The transformation preserves the angular momentum, $j = j_2$. Equation 43 concludes the second step in our transformation procedure.

At this stage, the angular dependence of the source term is represented partly in the mixed DVR−FBR representation of region 2, $s(i, v_2, j, \kappa) \equiv s(n, m, v_2, \alpha, j, \kappa)$. In the third step, we use the reverse of eq 18 to transform the source term to the angular FBR of region 2, $s(n, m, v_2, L, j, \kappa)$.

The final step is to transform the vibrational basis of AB labeled by v_2 to the FBR of region 2. In general, if different reference potentials are used to define the basis in different regions, this is achieved using the overlap matrix between the two sets of the FBR functions. The source term is now in the primary basis of region 2 and can be used with the propagation formula in eq 26.

For the OH + H_2 example considered in section III, the number of points i that map onto the area spanned by the reflecting potential is 10^5. The first step of the transformation therefore involves large transformation matrices and is the most time-consuming step. The second step is then performed typically for 10^5 different angles β, which lie in $\beta \in [0, \pi]$. The transformation matrices are small, since the transformation preserves j_2, and we precompute them on a dense (equally spaced) grid of β. The matrix elements for each $\beta(i)$ are determined on the fly by linear interpolation. This prescription saves the memory for storing the vast number of transformation matrices and avoids the explicit evaluation of Wigner d -matrix elements on the fly.

The transformation procedure is easily generalized to all pairs of arrangements with the nonreacting AB bond, AB + CD, ABC + D, and ABD + C. The 3-dimensional transformation of bond-forming and bond-breaking radial coordinates and the angle between them is accomplished using the kinematic rotation relations. The angular transformation matrices and the corresponding angles β are defined in Table 1 and Figure 5, respectively.

The 4-step procedure is a major improvement over evaluating the entire 6-dimensional source directly on the region 2 grid (at

TABLE 1: Parity-Adapted Transformation Matrices between the Coefficients Associated with Region 1 (I), Region 2 (II) and Region 3 (III) Angular Bases, $|j,(k, \kappa, \kappa')\rangle$, Respectively[a]

transformation	rotation matrix
I → II	$N_{\kappa k}[(-1)^{j+\kappa}d^j_{k-\kappa}(\beta) + \epsilon(-1)^k(-1)^{j+\kappa}d^j_{-k-\kappa}(\beta)]$
II → I	$N_{k\kappa}[(-1)^{j+k}d^j_{-k\kappa}(\beta) + \epsilon(-1)^\kappa(-1)^{j+k}d^j_{-k-\kappa}(\beta)]$
I → III	$N_{\kappa' k}[(-1)^j d^j_{-\kappa' k}(\beta) + \epsilon(-1)^k(-1)^j d^j_{-\kappa'-k}(\beta)]$
III → I	$N_{k\kappa'}[(-1)^j d^j_{-k\kappa'}(\beta) + \epsilon(-1)^{\kappa'}(-1)^j d^j_{-k-\kappa'}(\beta)]$
II → III	$N_{\kappa'\kappa}[(-1)^{\kappa'}d^j_{\kappa'\kappa}(\beta) + \epsilon(-1)^\kappa(-1)^{\kappa'}d^j_{\kappa'-\kappa}(\beta)]$
III → II	$N_{\kappa\kappa'}[(-1)^\kappa d^j_{\kappa\kappa'}(\beta) + \epsilon(-1)^{\kappa'}(-1)^\kappa d^j_{\kappa-\kappa'}(\beta)]$

[a] The angle β is defined in Figure 3, $0 \le \beta \le \pi$. $N_{k\kappa} = 1/[(1 + \delta_{k0})^{1/2}(1 + \delta_{\kappa 0})^{1/2}]$.

every time step at which the wave packet overlaps the reflecting potential). The transformation time in our OH + H_2 calculations takes a small fraction (<5%) of a propagation time step, which makes the RPD approach for 4-atom reactions very efficient.

The efficiency of the approach is based on our ability to divide the degrees of freedom into those which actively participate in the reaction and the spectator (nonreacting) degrees of freedom. The bond-forming and bond-breaking coordinates and the angle between them are interpolated directly. This is the most time-consuming step in the transformation, but it is tractable since the basis set in region 1 is very small. The spectator degrees of freedom use the same radial coordinates in both regions, while their angular part is described using the angular momentum eigenfunctions which can simply be rotated to another frame of axes.

It should also be noted that the application of the RPD method is made more effective by the localized nature of DAF basis functions. Figure 6 shows a comparison between a DAF basis and the sinc-DVR functions.[40] Since the nodes of the DAF/DVR functions functions of region 1 do not fall on the grid points in region 2, we also need to place the "tails" of the DAF/DVRs on the region 2 grid. This means that it is more efficient to perform the coordinate transformation using DAFs than the sinc-DVR basis.

F. Final State Analysis. We have now given the theory describing how to propagate a wave packet for a 4-atom system in time. To complete the theory, we need to specify the initial wave packet and the formulas to extract the reaction probabilities after the propagation. In order to do this, we use the time-independent wave packet approach.[49]

The initial state of the reactants is specified by the CD (H_2) and AB (OH) rovibrational quantum numbers (v_i, j_i), $i = 1$ and 2, respectively, and the orbital angular momentum quantum number, $l_i = j_{12,i}$. The wave packet is constructed in the form of eq 10) as a direct product of the internal molecular state and a Gaussian, $\tilde{\chi}(R) = R\chi(R)$, in the scattering coordinate R,

$$\tilde{\chi}(R|t=0) = \frac{1}{\sqrt{R_l \pi^{1/2}}} \exp\left(-\frac{(R - R_0)^2}{2R_l^2}\right) \exp(-ik_{\mathrm{av}}R) \quad (44)$$

where R_0 is the position of the center of the Gaussian, R_l is its width, and k_{av} is the average value of the momentum.

The time-independet wave packet, $\tilde{\xi}(E) = R\xi(E)$, is obtained by the half-Fourier time-to-energy transform,

$$\tilde{\xi}(E) = \frac{1}{2\pi}\int_0^\infty \mathrm{d}t\, \mathrm{e}^{\mathrm{i}Et}\tilde{\chi}(t) \quad (45)$$

On the potential side of the initial wave packet, $\tilde{\xi}(E)$ is related to the time-independent solution of the Schrdinger equation with the usual outgoing boundary conditions[49] through

$$\tilde{\psi}^+(E) = \frac{\sqrt{v_i}}{B^+_{l_i}(k_i)}\tilde{\xi}(E) \quad (46)$$

where

$$B^\pm_l(k) = \frac{1}{2\pi}\int_0^\infty \tilde{h}^\pm_l(kR)\,\tilde{\chi}(R)\,\mathrm{d}R \quad (47)$$

The radial part of the asymptotic wave function is

$$\tilde{\psi}^+(R) = \sum_f \left(\frac{\tilde{h}^-_{l_i}(k_i R)}{\sqrt{v_i}}\delta_{if} - S_{f\leftarrow i}\frac{\tilde{h}^+_{N_f}(k_f R)}{\sqrt{v_f}}\right) \quad (48)$$

where $\tilde{h}^\pm$ are Ricatti−Hankel functions. E is the total initial energy, S is the scattering matrix, $k_{i,f}$ and $v_{i,f}$ are the initial and final wave vectors and velocities for motion along the scattering coordinate (in region 1 and 2, respectively), e.g.

$$k_i = \sqrt{2\mu_R(E - \epsilon_{v_1 j_1} - \epsilon_{v_2 j_2})} \quad (49)$$

and $\epsilon_{v_i j_i}$ are the energies of the initial diatom rovibrational states. The indices i denote collectively all the initial quantum numbers, $(v_{1,i},\ j_{1,i},\ v_{2,i},\ j_{2,i},\ l_i = j_{12})$. The final quantum numbers are collectively denoted by f; in the product arrangement, they are (N, L, t), where t sums over all final triatom states with total triatom angular momentum L.

The total probability of a reaction is determined by calculating the outgoing flux in the product arrangement through a dividing surface $R = R_*$,

$$J = \frac{1}{\mu_R}\mathrm{Im}\,\langle\tilde{\psi}^+|\frac{\mathrm{d}}{\mathrm{d}R}|\tilde{\psi}^+\rangle\Big|_{R=R_*} \quad (50)$$

The wave function and its derivatives at R_* are calculated using eqs 45 and 46, where the time integrals are cumulatively built throughout the propagation. The first derivative of a wave packet is evaluated using the derivative of a DAF, which is analytic, and eq 12.

State-to-state probabilities are determined by calculating the overlap with a probe packet $\tilde{\chi}_f$, which is a product of internal an internal triatom state and a Gaussian placed in the asymptotic region. The energy content in the probe wave packet must have a significant amplitude at the product kinetic energies that correspond to the total collision energies of interest.

The triatom states are determined using the same basis functions in r, ρ, and γ as those used in region 3 to represent the wave packet. The physical parity of the 4-atom system ϵ is related to the physical parity of the triatom, ϵ_t, by

$$\epsilon = \epsilon_t(-1)^L \quad (51)$$

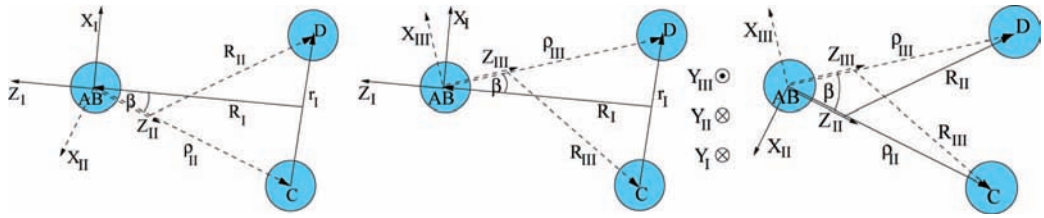

Figure 5. Diagram that defines angles β for step 2 of the reagent-to-product coordinate transformation applied to the source terms $-W\chi_1(t)$ between arrangements: I, AB + CD; II, ABC + D; and III, ABD + C. Transformation matrices using angles β as arguments are defined in Table 1.

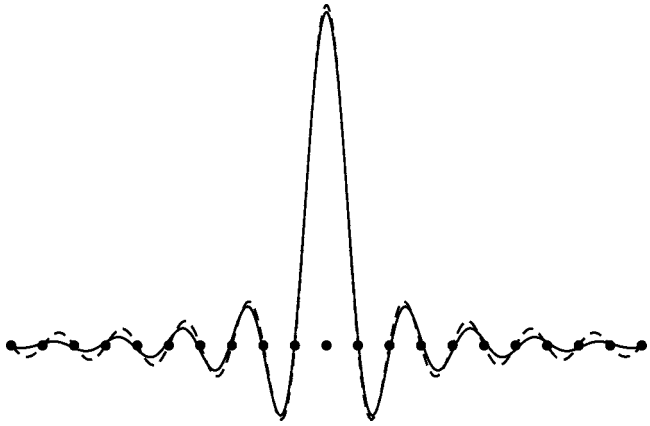

Figure 6. Comparison of the 1-D interpolation matrix corresponding to the distributed approximating functional (DAF) (solid line) used in our calculations and DVR (dashed line) representations of the equally space radial grids. In the notation of ref 54 the DAF parameters are $M = 150$ and $\sigma(0) = 4\Delta R$. The DAF is narrower which gives added efficiency in the reagent-to-product coordinate transformation. The spacings used between the grid points are given in Table 2.

TABLE 2: Parameters Used in the Wave Packet Calculations of Section III[a]

description	parameter	value/au
χ_0 parameters	R_0, R_l, k_{av}	7.5, 0.5, 9
χ_f parameters	R_f, R_l, k_{av}	12, 0.23, 12.5
flux calculation plane	R_*	6.5
no. of iterations	N_{it}	1400
time step	Δt	8
width of absorbing potentials	ΔR_{abs}	3
width and height of reflecting potential	W_{ramp}, ΔR_w	0.5, 1.5
planes of no return	P_1, P_2	6.5, 5.5
equal grid spacings	$\Delta R_{reg1,2,3}$, $\Delta\rho$	0.08
vibrational FBR limits, region 1	$v_{1,max}$, $v_{2,max}$	2, 0
vibrational FBR limits, region 2	v_{max}	0
vibrational FBR limits, region 3	$v_{\rho,max}$, v_{max}	5, 0
angular FBR limits, region 1	j_{1max}, j_{2max}	3, 1
angular FBR limits, region 2	L_{max}, j_{max}	55, 1
angular FBR limits, region 3	L_{max}, j_{max}	45, 1

[a] All symbols are defined in the text.

From the overlaps of the time-independent wave packet with the probe packet, one obtains state-to-state probabilities, $|S_{f\leftarrow i}|^2$, using

$$S_{f\leftarrow i} = \frac{-\sqrt{v_i v_f}}{2\pi B_{l_i}^{+}(k_i) B_{N_f}^{-}{}^{*}(k_f)} \langle \tilde{\chi}_f | \tilde{\xi} \rangle \qquad (52)$$

with $B^{\pm}(k_{i,f})$ defined with eq 47, where the integration involves the initial and probe wave packet, respectively.

III. Test Calculations

In this section we report numerical calculations that were carried out to demonstrate the efficiency and accuracy of the RPD approach of section II. All calculations were carried out on the benchmark OH(v=0, j=0) + H$_2$(v=0, j=0) reaction, using the Wu−Schatz−Lendvay−Fang−Harding (WSLFH) potential energy surface.[34] The WSLFH potential is a fit of ab initio data to an analytic expression. We symmetrized it with respect to all hydrogen exchanges. The reaction has a barrier in the reactant arrangement of approximately 0.24 eV and is exoergic by 0.70 eV. The zero-point energy of the reactants is 0.497 eV.

Since these were test calculations, we limited the vibrational OH basis to the zero-point motion, $v_{2,max} = 0$, and its rotational basis to $j_{2,max} = 1$, to reduce the computational effort. The properties we wish to test (such as the RPD coordinate transformation) do not depend strongly on the quantum numbers of the OH fragment, (v_2, j_2), since the rovibrational basis of OH is the same in both regions, except for a rotation of the quantization axis. In order to converge the potential matrix elements, we use a larger angular GDVR grid, $(j_{1,max} + 1) \times 13 \times 5$ (in γ, θ, and χ), than the number of FBR functions in each degree of freedom (e.g., two γ angles are not sufficient to converge potential matrix elements involving $j_2 = 0,1$).

The consequence of using a basis which is not fully converged with respect to j_2 is that $e^{-iV\Delta t}$ is not unitary. One way round this problem is to diagonalize the potential matrix at each radial grid point, prestore the transformation matrices, and evaluate the $e^{-iV\Delta t}$ at each time step by transforming to its diagonal representation and back. This procedure is extremely time consuming for large angular basis sets and the storage requirements, even for the $j_{2,max} = 1$ basis, are 11 GB. Therefore, we used the alternative approach of evaluating the term by performing a short iterative Lanczos propagation[59] for each radial grid point, which is automatically unitary. An expansion to eighth order was necessary to converge the $\Delta t = 8$ au calculations. This (unnecessarily expensive) evaluation of the $e^{-iV\Delta t}$ term for a nonconverged angular basis has been corrected for in all the timing estimates given below.

A. Overall Efficiency of the RPD Scheme. To test the partitioning at the start of the reagent channel, we computed initial state-selected reaction probabilities for the reaction OH(v=0, j=0) + H$_2$(v=0, j=0) and compared with the results obtained by solving the exact (i.e., unpartitioned) Schrödinger equation using product coordinates throughout regions 1 and 2.

The basis set and other parameters used in the converged partitioned calculation are given in Table 2. The initial Gaussian wave packet covers the range of energies up to ≈ 0.75 eV. The results are plotted in Figure 7. The partitioned calculation used $j_{1,max} = 55$. The unpartitioned calculations with $j_{1,max} = 65$ and 95 are shown for comparison. The unpartitioned calculations also require a larger equidistant grid in R and ρ, which extends to 14.5 au to accommodate the initial wave packet and the absorbing potential beyond it. The reaction probabilities for $j_{1,max} = 95$ show excellent agreement with the partitioned calculation over the full energy range.

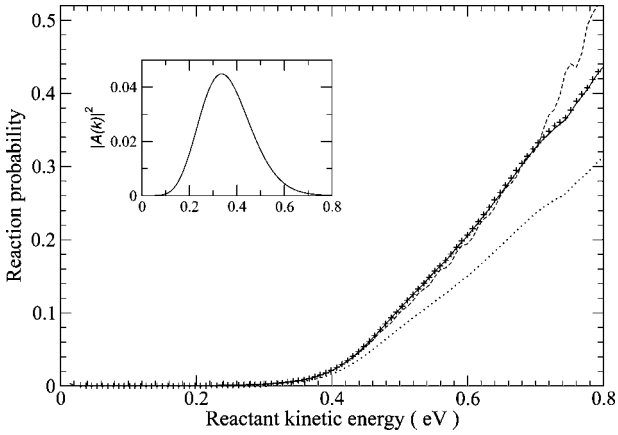

Figure 7. Comparison of total reaction probabilities for OH(v=0, j=0) + H_2(v=0, j=0) computed by applying the RPD approach of this article (solid line) and by solving the exact (i.e., unpartitioned) Schrödinger equation with $j_{1,max} = 65$ (dashed line) and $j_{1,max} = 95$ (pluses). Also shown are the results obtained for the same time step $\Delta t = 8$ au (dotted line) using the earlier RPD approach of ref 26. Inset shows the energy content of the initial wave packet.

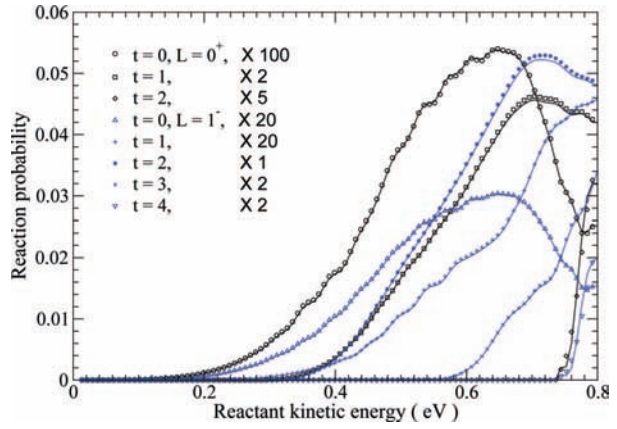

Figure 8. State-to-state reaction probabilities computed for the reaction OH(v=0, j=0) + H_2(v=0, j=0) → H + H_2O(t,L) using the RPD approach of this article (solid line) and using an unpartitioned propagator (symbols).

The bottleneck in the time propagation is the evaluation of the potential matrix elements. Almost all the time is spent on transforming the angular FBR to the GDVR and back. Since in our tests, the unpartitioned calculation has almost double the number of points on the radial $R \times \rho$ grid, the angular FBR-DVR transformation is done 2 times more than in the RPD scheme, and the matrices involved in the transformation are ≈70% (96/56) larger than in the RPD scheme. In the limit of a large basis, this makes the angular FBR-GDVR transformations 6 times slower in the unpartitioned calculations than in the RPD scheme, which results in a 6 times longer total execution time.

To further test the accuracy of the RPD approach, we included region 3 in both calculations. Region 3 gives us more room to propagate the wave packet beyond the plane of no return, and to perform the state-to-state analysis with only a negligible amount of additional effort. Figure 8 shows a selection of the OH(v=0,j=0) + H_2(v=0,j=0) state-to-state reaction probabilities (for all accessible H_2O bound states with $L = 0$ and 1), calculated using the RPD method using the parameters of Table 2. The bound-state energies of the final states shown are in Table 3. The results of the partitioned calculation are presented with a full line, and the symbols represent the unpartitioned results. Both agree well over the full energy range,

TABLE 3: Bound-State H_2O Energies (in eV): $v_{2,max} = 0$, $j_{2,max} = 1$

t, L	energy/eV
0, 0^+	1.020
1, 0^+	1.486
2, 0^+	1.933
0, 1^-	1.024
1, 1^-	1.296
2, 1^-	1.490
3, 1^-	1.720
4, 1^-	1.937

with discrepancies slightly larger than for the total reaction probabilities. The state-to-state probabilities are small and very sensitive to the details of the calculation and they present the most rigorous test for our RPD methodology. Transformation to region 3 requires no change of coordinates and its inclusion allows us to contract the range in the R coordinate in the unpartitioned calculation by ≈20%.

B. The Reactant−Product Coordinate Transformation. To make the partitioned calculations most efficient, one needs to use the smallest possible basis in region 1 that is sufficient to describe the propagation without the reflecting potential. The radial grid spacings and angular γ grid in region 2 are the parameters used to converge the norm of the interpolated source in region 2. This interpolation is facilitated by making the region 1 basis as small as possible. We first tried to use a step potential for the reflecting potential in region 1, but we found that such a reflector induced high-energy oscillations in the colliding wave packet that lay outside the energy range of our radial DAF. In our test calculation, this resulted in a 5% reduction in the wave packet norm in region 1 following collision with the reflecting potential, and a similar loss of norm in the interpolation of the region 2 source terms. The reflecting potential in eq 34 conserves the interpolation norm, using the basis described above, to 1 part in 10 000. It also reflects the incoming wave packet more effectively, which allows it to be made slightly thinner (by 0.3 au) and the time that it is overlapped by the wave packet is shorter by ≈5%. With this choice of reflecting potential, no reduction in the time step is necessary in comparison with an unpartitioned calculation.

The interpolation is performed at every time step, but in our test calculations it amounts to less than 5% of a propagation step and needs to be performed in ≈200 propagation steps. In a fully converged calculation, this time will be about the same or less. To deduce this, we compare the cost of interpolation to the most time-consuming angular FBR-to-DVR transformation. The increase in the rotational basis with $j_{2,max}$ does not affect the size of the transformation matrices in step 1 of the coordinate transformation in eq 41. So if in our test calculations the interpolation takes a shorter time than the first step in the angular FBR-to-DVR transformation, eq 18, it will do so by a similar ratio for a larger rotational basis of OH, since the number of matrix multiplications is proportional to the size of OH basis, but the dimension of the matrices is not. The number of rotations in step 2 of the coordinate transformation, eq 43, is proportional to the number of points on the (R, ρ, γ) grid, which is a fraction of the full region 2 grid (in these degrees of freedom). In comparison with the last step in the angular FBR-to-DVR transformation, involving the matrix $T_{k,\gamma}$, the transformation is done fewer number of times and involves matrices that are smaller or equal (for $j_2 = j_{2,max}$) to $T_{k,\gamma}$. Following a similar argument, we deduce that step 3 of the coordinate transformation takes less time than step 1 of the angular DVR-to-FBR

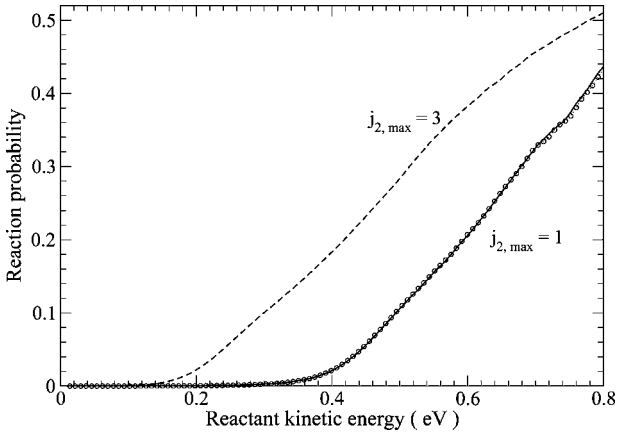

Figure 9. Total reaction probabilities for OH(v=0, j=0) + H_2(v=0, j=0) with $j_{2,max}$ = 1 computed using the RPD approach (solid line) and the squeezed wave packet approach (circles). The RPD reaction probabilities with $j_{2,max}$ = 3 are shown using dashed line.

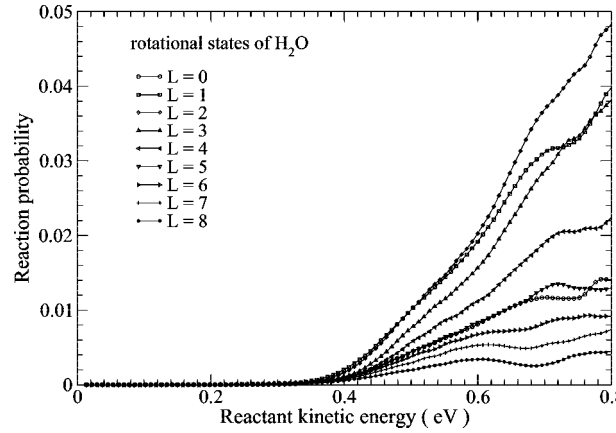

Figure 10. Energy dependence of different final H_2O rotational states L for OH(v=0, j=0) + H_2(v=0, j=0) → H + H_2O(t, L) with $j_{2,max}$ = 1.

transformation. Hence we can be confident that the time taken by the interpolation will never exceed 5% of the propagation time.

C. Comparison with Related Methods. ***1. Partitioning of the Schrödinger Equation.*** As explained in section IIB, the partitioning is implemented directly into the split-operator propagator, following eqs 6 and 7, rather than into the time-dependent Schrödinger equation. The latter is less efficient because it gives an additional error in the propagation that scales as Δt^2 instead of Δt^3. With a time step sufficient for convergence, this additional error turns out to be significant, and is illustrated in Figure 7 (dotted line). A much smaller time step would be required for the Schrödinger-partitioned version of the propagator to yield a converged answer. This result demonstrates clearly why one should partition the propagator and not the time-dependent Schrödinger equation.

2. "Squeezed" Wave Packet Approach. An alternative approach to the RPD scheme is to propagate the wave packet in region 1 until it approaches the interaction region and then to transform the whole wave packet to the region 2 grid in one step.[60] We implemented this approach and found that, for the WSLFH potential, it is possible to perform the calculations with similar accuracy and efficiency to the RPD approach. We use a "squeezed" wave packet, which is propagated backward from R = 4 au to R = 10 au in the absence of the potential, so as to localize the wave packet upon entrance of region 2. We propagate the wave packet forward in time for 1760 au (220 iterations). The propagation time in region 1 needs to be carefully chosen, so that the parts of the wave packet reflected back beyond the plane of no return P_2 and the high-energy components that traverse the barrier toward products are negligible. The reaction probabilities are shown using circles in Figure 9. There are small discrepancies at the high-energy end of the studied range which we found difficult to remove. Using an equidistant grid in r_1 would possibly yield a slightly better representation in region 1. The discrepancies are larger in the state-to-state probabilities (not shown) in comparison with the differences between the unpartitioned and the above RPD results.

As discussed above, the bottleneck of all the calculations (in the limit of a large basis set) is the propagation in region 2. The extent of region 2 is determined by the positions of the planes-of-no-return, and it determines the basis set size and the computational effort of the whole calculation. The main advantage of using the squeezed wave packet approach is that it requires less iterations in region 2, since the initial propagation is performed in region 1 only. However, this approach can only be applied when the interactions in the reactant arrangement allow the wave packet in region 1 to be propagated inside region 2 without spreading beyond the plane of no return P_2. In our test calculations, it turned out that we needed to extend the ρ grid by about 15% in comparison with the region 2 basis in our RPD calculations in order to accommodate the entire wave packet in region 2. This would make the squeezed wave packet calculations more expensive for a larger OH rotational basis.

The RPD approach advocated in this paper is our preferred choice, since it yields an automatic procedure for obtaining converged reaction probabilities, and is more general, since it is less sensitive to the entrance channel interactions. We can be confident of the results if the wave packet does not penetrate the reflecting potential (which is tested at end points of the region 1 grid), if the interpolation conserves the source norm, and if our results are insensitive to the position of the reflecting and absorbing potentials in the reactant arrangement.

D. Further Tests of the RPD Approach. Apart from the state-to-state reaction probabilities, it is easy to compute the distribution of final H_2O rotational states without calculating the H_2O bound states by resolving the flux in eq 50. This is shown in Figure 10. The rotational distributions peak at L = 2 at all collision energies.

We also applied the RPD method to calculate the total reaction probabilities for $j_{2,max}$ = 3 in Figure 9. We used all parameters in Table 2 unchanged, with the angular GDVR grid slightly increased to 56 × 15 × 7 (in γ, θ, and χ, respectively). The reaction threshold is at considerably lower kinetic energies because of the zero-point-energy dependence on the OH rotational basis. This is also reflected in the bound state energies of H_2O in Table 4. The higher reactivity is due to the larger number of accessible states for the larger basis. The state-to-state probabilities with $j_{2,max}$ = 3 are shown in Figure 11. All results were calculated at little additional effort on top of what was required to compute the total reaction probability. They are converged with respect to all basis set parameters (except $v_{2,max}$ and $j_{2,max}$) and the locations of the reagent and product points-of-no-return. The results shown were found to be insensitive (to within graphical accuracy) to variation in these parameters, thus demonstrating that the RPD method has successfully converged the state-to-state reaction probabilities.

The extension of this method to treat partial waves with higher total angular momentum J using the method of ref 48 is underway. With the parallelisation of the angular FBR-DVR

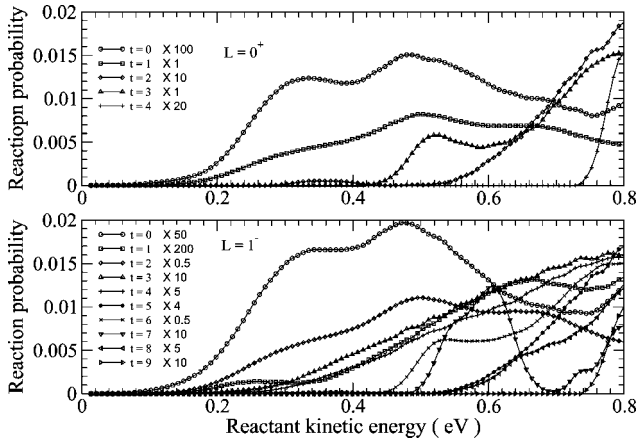

Figure 11. State-to-state reaction probabilities computed using the RPD approach for the reaction $OH(v=0, j=0) + H_2(v=0, j=0) \rightarrow H + H_2O(t,L)$ with $j_{2,max} = 3$.

TABLE 4: Bound State H_2O Energies (in eV): $v_{2,max} = 0$, $j_{2,max} = 3$

t, *L*	energy/eV
0, 0^+	0.695
1, 0^+	1.153
2, 0^+	1.461
3, 0^+	1.588
4, 0^+	1.931
0, 1^-	0.700
1, 1^-	0.801
2, 1^-	1.157
3, 1^-	1.240
4, 1^-	1.266
5, 1^-	1.466
6, 1^-	1.593
7, 1^-	1.682
9, 1^-	1.935

transformations, fully converged calculations and comparisons of state-to-state cross sections with experiment will be within reach.

IV. Conclusions and Outlook

In this article we have developed and tested an efficient method for computing state-to-state scattering properties for reactions of type AB + CD → ABC + D. The method is an extension to 4-atom reactions of a version of the reactant−product decoupling (RPD) approach, developed in earlier work[28] on 3-atom reactions. It involves a number of new theoretical algorithms which were necessary to overcome the challenges of extending the RPD approach from 3-atom to 4-atom reactions. In particular, the split-operator propagator is by far the most efficient propagator in a 4-atom reaction (since the discretization transformation in the angular basis is not orthogonal), and we found that it is much more efficient to partition the propagator itself rather than the time-dependent Schrödinger equation. We also showed that the reagent-to-product coordinate transformation can be carried out in four stages, which reduces the amount of computer time required for this procedure to a small fraction of the total propagation time. Numerical tests on the OH + H_2 reaction have confirmed the accuracy and efficiency of the new RPD approach and demonstrate that it will allow very accurate and efficient benchmarking calculations to be carried out on this and other 4-atom reactions in the near future.

Acknowledgment. This research was funded by a grant from the UK Engineering and Physical Sciences Research Council (EPSRC) and was carried out as part of a CCP6 "Flagship Project". M.T.C. also thanks Sidney Sussex College for financial support.

References and Notes

(1) Althorpe, S. C.; Clary, D. C. *Annu. Rev. Phys. Chem.* **2003**, *54*, 493.
(2) Liu, K. *Annu. Rev. Phys. Chem.* **2001**, *52*, 139.
(3) Althorpe, S. C.; Fernández-Alonso, F.; Bean, B. D.; Ayers, J. D.; Pomerantz, A. E.; Zare, R. N.; Wrede, E. *Nature* **2002**, *416*, 67.
(4) Harich, S. A.; Dai, D.; Wang, C. C.; Yang, X.; Chao, S. D.; Skodje, R. T. *Nature* **2002**, *419*, 281.
(5) Juanes-Marcos, J. C.; Althorpe, S. C.; Wrede, E. *Science* **2005**, *309*, 1227.
(6) Che, L.; Ren, Z.; Wang, X.; Dong, W.; Dai, D.; Wang, X.; Zhang, D. H.; Yang, X.; Sheng, L.; Li, G.; Werner, H.-J.; Lique, F.; Alexander, M. H. *Science* **2007**, *317*, 1061.
(7) Neuhauser, D.; Baer, M.; Judson, R. S.; Kouri, D. J. *J. Chem. Phys.* **1989**, *90*, 5882.
(8) Manthe, U.; Seideman, T.; Miller, W. H. *J. Chem. Phys.* **1993**, *99*, 10078.
(9) Manthe, U.; Seideman, T.; Miller, W. H. *J. Chem. Phys.* **1994**, *101*, 4759.
(10) Pogrebnya, S. K.; Echave, J.; Clary, D. C. *J. Chem. Phys.* **1997**, *107*, 8975.
(11) Pogrebnya, S. K.; Palma, J.; Clary, D. C.; Echave, J. *Phys. Chem. Chem. Phys.* **2000**, *2*, 693.
(12) Zhang, D. H.; Collins, M. A.; Lee, S.-Y. *Science* **2000**, *290*, 5493.
(13) Zhang, D. H. *J. Chem. Phys.* **2006**, *125*, 133102.
(14) Zhang, D. H.; Zhang, J. Z. H. *J. Chem. Phys.* **1995**, *120*, 6512.
(15) Zhang, D. H.; Zhang, J. Z. H.; Zhang, Y.; Wang, D.; Zhang, Q. *J. Chem. Phys.* **1995**, *102*, 7400.
(16) Zhang, D. H.; Light, J. C. *J. Chem. Phys.* **1996**, *104*, 4544.
(17) Zhang, D. H.; Yang, M.; Lee, S.-Y. *Phys. Rev. Lett.* **2002**, *89*, 103201.
(18) Zhang, D. H.; Xie, D.; Yang, M.; Lee, S.-Y. *Phys. Rev. Lett.* **2002**, *89*, 283203.
(19) Zhu, W.; Dai, J.; Zhang, J. Z. H.; Zhang, D. H. *J. Chem. Phys.* **1996**, *105*, 4881.
(20) Zhang, D. H.; Lee, S.-Y. *J. Chem. Phys.* **1999**, *110*, 4435.
(21) Goldfield, E. M.; Gray, S. K. *J. Chem. Phys.* **2002**, *117*, 1604.
(22) Mayneris, J.; González, M.; Gray, S. K. *Comput. Phys. Commun.* **2008**, *179*, 741.
(23) Medvedev, D. M.; Gray, S. K.; Goldfield, E. M.; Lakin, M. J.; Troya, D.; Schatz, G. C. *J. Chem. Phys.* **2004**, *120*, 1231.
(24) Valero, R.; McCormack, D. A.; Kroes, G.-J. *J. Chem. Phys.* **2004**, *120*, 4263.
(25) Hu, W.; Schatz, G. C. *J. Chem. Phys.* **2006**, *125*, 132301.
(26) Peng, T.; Zhang, J. Z. H. *J. Chem. Phys.* **1996**, *105*, 6072.
(27) Althorpe, S. C.; Kouri, D. J.; Hoffman, D. K. *J. Chem. Phys.* **1997**, *107*, 7816.
(28) Althorpe, S. C. *J. Chem. Phys.* **2001**, *114*, 1601.
(29) Althorpe, S. C. *Int. Rev. Phys. Chem.* **2004**, *23*, 219.
(30) Juanes-Marcos, J. C.; Althorpe, S. C. *Chem. Phys. Lett.* **2003**, *381*, 743.
(31) Panda, A. N.; Althorpe, S. C. *Chem. Phys. Lett.* **2006**, *419*, 245.
(32) Tal-Ezer, H.; Kosloff, R. *J. Chem. Phys.* **1984**, *81*, 3967.
(33) Feit, M. D.; Fleck, J. A. *J. Chem. Phys.* **1983**, *78*, 301.
(34) Wu, G.-S.; Schatz, G. C.; Lendvay, G.; Fang, D.-C.; Harding, L. B. *J. Chem. Phys.* **2000**, *113*, 3150.
(35) Lee, H.-S.; Light, J. C. *J. Chem. Phys.* **2003**, *118*, 3458.
(36) Lee, H.-S.; Light, J. C. *J. Chem. Phys.* **2004**, *120*, 4626.
(37) Mladenović, M. *J. Chem. Phys.* **2000**, *112*, 1070.
(38) Manolopoulos, D. E. *J. Chem. Phys.* **2002**, *117*, 9552.
(39) Gonzales-Lezana, T.; Rackham, E. J.; Manolopoulos, D. E. *J. Chem. Phys.* **2004**, *120*, 2247.
(40) Colbert, D. T.; Miller, W. H. *J. Chem. Phys.* **1992**, *96*, 1982.
(41) Meyer, R. *J. Chem. Phys.* **1970**, *52*, 2053.
(42) Muckerman, J. T. *Chem. Phys. Lett.* **1990**, *173*, 200.
(43) Dickinson, A. S.; Certain, P. R. *J. Chem. Phys.* **1968**, *49*, 4209.
(44) Corey, G. C.; Tromp, J. W. *J. Chem. Phys.* **1995**, *103*, 1812.
(45) Corey, G. C.; Lemoine, D. *J. Chem. Phys.* **1992**, *97*, 4115.
(46) Press, W. H. Flannery, B. P. Teukolsky, S. A. Vetterling, W. T. *Numerical Recipes*; Cambridge University Press: Cambridge, UK, 1988.
(47) Zare, R. N. *Angular Momentum*; Wiley: New York, 1988.
(48) Cvitaš, M. T.; Althorpe, S. C. *Comput. Phys. Commun.* **2007**, *157*, 357.
(49) Kouri, D. J.; Hoffman, D. K. *Few-Body Systems* **1995**, *18*, 203.
(50) We use the term "primary representation", or "primary basis", to denote the representation in terms of which the wave packet is stored in the computer memory.

(51) Bačić, Z.; Light, J. C. *J. Chem. Phys.* **1986**, *85*, 4594.

(52) Gatti, F.; Iung, C.; Menou, M.; Justum, Y.; Nauts, A.; Chapuisat, X. *J. Chem. Phys.* **1998**, *108*, 8804.

(53) Gatti, F.; Iung, C.; Menou, M.; Chapuisat, X. *J. Chem. Phys.* **1998**, *108*, 8821.

(54) Huang, Y.; Zhu, W.; Kouri, D. J.; Hoffman, D. K. *J. Phys. Chem.* **1994**, *98*, 1868.

(55) Leforestier, C.; Bisseling, R. H.; Cerjan, C.; Feit, M. D.; Friesner, R.; Guldberg, A.; Hammerich, A.; Jolicard, G.; Karrlein, W.; Meyer, H. D.; Lipkin, N.; Roncero, O.; Kosloff, R. *J. Chem. Phys.* **1991**, *94*, 59.

(56) This follows because $[(2l + 1)/(2J + 1)]^{1/2}\langle l0,j_{12}\Omega|J\Omega\rangle = (-1)^l$.

(57) Equation 30 is a special case of the body-fixed primitive basis $\tilde{D}^J_{M\Omega}(\mathrm{SF}\rightarrow\mathrm{BF})\tilde{D}^J_{\Omega\kappa}(0,\gamma,\chi)\Theta_{j\kappa}(\theta)$, for $J = M = \Omega = 0$, where $\tilde{D}^J$ are normalized Wigner rotation matrices, using $\tilde{d}^L_{0\kappa} = \Theta_{L-\kappa}$. Euler angles (0, γ, χ) bring the BF frame to the molecular frame, with z axis pointing along $\boldsymbol{\rho}$ vector and $\mathbf{r}$ in the positive x half of the xz plane.

(58) One can reduce the size of the wave packets in the Chebyshev approach by using the real wave packet method [Gray, S. K.; Balint-Kurti, G. G. *J. Chem. Phys.* **1998**, *108*, 950], although this approach has the effect of making less efficient the transformation from reagent-to-product coordinates of the RPD source-terms.

(59) Park, T. J.; Light, J. C. *J. Chem. Phys.* **1986**, *85*, 5870.

(60) Zhang, J. Z. H. *Theory and Application of Quantum Molecular Dynamics*; World Scientific: Singapore, 1999.

(61) This is a consequence of the coordinate problem, that the number of product-arrangement basis functions required to describe the wave packet increases with increasing reagent separation.

JP8111974